Angular distributions for the $^{12}C(\gamma,p)^{11}B$ reaction

H. Ruijter, J-O. Adler, B-E. Andersson, K. Hansen, L. Isaksson, and B. Schrøder
Department of Physics, University of Lund, Sölvegatan 14, S-223 62 LUND, Sweden

J. Ryckebusch, D. Ryckbosch, L. van Hoorebeke, and R. van de Vyver
Laboratory for Nuclear Physics, University of Gent, Proeftuinstraat 86, B-9000 Gent, Belgium

(Received 5 July 1995; revised manuscript received 30 August 1996)

Absolute differential cross sections for the $^{12}C(\gamma,p)^{11}B$ reaction have been measured for low-lying regions of residual excitation energy in ^{11}B. Cross sections with low systematic uncertainties are presented for proton detection angles ranging from 30° to 150°, measured with tagged photons of 25–75 MeV energy. The experimental results resolve the discrepancies between the older data sets. In addition, a reinterpretation of the low-lying states excited in ^{11}B is presented. It is concluded that HF-RPA calculations with essential contributions of meson exchange currents (MEC) provide a qualitative description of the angular distributions obtained for the negative parity states in the (γ,p) reaction. [S0556-2813(96)04712-7]

PACS number(s): 25.20.−x, 27.20.+n

INTRODUCTION

The combination of high-duty-factor electron beams and the tagging technique [1] has led to a large number of photonuclear experiments which are an improvement upon previous bremsstrahlung measurements. The data sets produced with tagged photons and new product particle detectors have brought about renewed interest in the study of the reaction mechanisms within more microscopic models. The early assumption of a direct-knock-out (DKO) mechanism [2] was questioned when it was shown that the cross sections for the (γ,p_0) and (γ,n_0) reactions were of similar magnitudes, and distorted-wave-impulse approximation (DWIA) calculations could not describe both reactions simultaneously [3–6]. The proposed quasideuteron (QD) model [7–9] was very successful in explaining the experimental cross sections and introduced the concept of photoabsorption on a correlated proton-neutron pair. The modified-quasideuteron (MQD) interpretation was introduced in order to explain how the momentum mismatch in the (γ,p) and (γ,n) reactions is overcome. The microscopic models that have been presented recently [10–12] introduce a formal description of the previous concepts. An attempt is made to incorporate shell model contributions, nucleonic correlations, and meson-exchange currents (MEC) in a consistent manner.

Photons produced with a single-difference bremsstrahlung technique were used in an early experiment by Matthews *et al.* [13]. The cross sections were compared with a direct-knock-out model in which photons were assumed to interact with protons both in the p and s shells in ^{12}C. Contrary to the $(e,e'p)$ case, no clear evidence was found for s-shell contributions which are instead believed to be part of the continuum region.

The measured (γ,p) cross sections were extended to higher excitation energies in the residual nucleus by McGeorge *et al.* [14]. Although the kinetic energy resolution of the protons was about the same as in the bremsstrahlung measurements, the use of tagged photons allowed higher excitation energy regions to be measured. In agreement with Matthews *et al.*, McGeorge *et al.* considered the DKO mechanism for high residual excitations to be highly unlikely.

A tagging spectrometer with 50 keV energy resolution in combination with silicon-germanium (Si-Ge) telescopes was used for the first time by Shotter *et al.* [15,16]. This setup revealed resolved low-lying excited states in ^{11}B which had not been accomplished before. A composite model including a modified-quasideuteron mechanism in addition to the DKO and the QD models was used in the interpretation of the results. Compared with the $(e,e'p)$ reaction at lower missing momentum, the (γ,p) reaction has large cross sections for states at $\sim$ 7 MeV in ^{11}B. The MQD mechanism was proposed in order to explain the strongly populated states as a photon interacting with two correlated nucleons, one being ejected and the other absorbing momentum into the recoiling nucleus. The peak at $\sim$ 7 MeV coincides with known levels in ^{11}B at 6.743 MeV $(7/2^-)$, 6.792 MeV $(1/2^+)$, and 7.286 MeV $(5/2^+)$. Since there was no evidence of the population of the 4.445 MeV $(5/2^-)$ state, it seemed improbable that the $(7/2^-)$ state would carry much strength, as both states are observed simultaneously in hadron reactions. Instead, it was assumed that population of the $(1/2^+)$ state would be more likely as there was no evidence of excitation of the $(5/2^+)$ state. Another measurement using Si-Ge detectors [17] led to results where a sizable contribution to the $\sim$7 MeV peak could be due to the $(5/2^+)$ state in addition to the $\sim$6.8 MeV states [18].

Previous interpretations of the measured cross sections have, to a large extent, been based on the quasideuteron model. Although total cross sections have been described, the model is not appropriate for angular distributions at forward angles. Recent work on the theoretical interpretation of (γ,N) reactions has made it possible to calculate single-hole (1h) transition matrix elements within the random phase approximation with exchange current effects included [11,12]. Transitions of two-hole–one-particle (2h1p) type are an extension in which one-pion exchange currents are explicitly accounted for. In these 2h1p calculations, however, it has not been possible to reach the same level of complexity as that obtained for the 1h transition where one-step reaction

mechanisms are accounted for. Calculations within this model [19] for ^{12}C can describe part of the data presented here.

In this paper, we present absolute differential cross sections for the $^{12}C(\gamma,p)^{11}B$ reaction at incident photon energies from 25 MeV to 78 MeV. Compared with previous measurements, the systematic uncertainty has been reduced considerably. An abundance of data has been available with higher systematic uncertainty. The data presented here seem to provide a mean value of previous measurements and are considered as a good constraint on theoretical predictions. Absolute differential cross sections for angular distributions, $30° < \theta_p < 150°$, with good energy resolution have been obtained in experiments at mean photon energies of 60 and 80 MeV. Angular distributions, $30° < \theta_p < 90°$, also are presented for photon energies in the range 42 to 56 MeV. Cross sections also have been obtained in the giant dipole resonance region, $40° < \theta_p < 120°$, for the ground-state transition.

The aim of the experiments was to provide cross sections for further investigations of the reaction mechanisms. Due to the relatively poor resolution obtained in previous experiments, there has been disagreement as to which states are actually excited in the reaction. Although the resolution for the excitation energy spectra presented here is of the same order as for other recent measurements, the statistical significance and the larger data set allowed a more systematic identification method to be used.

EXPERIMENTAL SETUP

All measurements were performed at the MAX laboratory in Lund, where a racetrack microtron and a pulse-stretcher ring provide an almost continuous electron beam [20–22]. The microtron accelerates a 100 keV electron beam to a maximum energy of 100 MeV which is injected by multiturn injection into the pulse-stretcher ring. With 0.4 μs pulses of 5 mA, and a repetition rate of 50 Hz, the maximum extracted current is 100 nA. The chromaticity is the same for electron beams of 75 and 95 MeV, but the synchrotron losses increase from 0.44 MeV to 1.12 MeV during the 20 ms extraction resulting in difficulties in keeping the ring filled for the entire period at the higher beam energy. A duty factor close to 1 thus can be obtained at 75 MeV, whereas a factor of 0.5 is normal at 95 MeV.

Two different magnetic spectrometers were used to detect residual electrons following bremsstrahlung radiation in aluminium foils 50 μm thick. In the first spectrometer with inclined pole faces [23], the focal plane was equipped with a 22-channel hodoscope consisting of NE102A plastic scintillation detectors placed inside the same vacuum chamber as the radiator. The energy resolution of each detector was 270 keV at an incident electron energy of 75 MeV, resulting in a tagged energy range of 6 MeV. With 95 MeV electrons, the corresponding tagged interval was 9 MeV. The spectrometer used at present is an Elbeck spectrometer and is similar to the one used in Mainz [24]. This spectrometer is equipped with 64 nonoverlapping scintillation detectors in the focal plane, grouped as 2 times 32, located on a rail outside the vacuum chamber. The two hodoscopes of this spectrometer can be moved independently and can be located anywhere from $E_\gamma = 0.1–0.8$ times the incoming electron energy. The photon energy resolution is 220 keV with a mean incident electron energy of 75 MeV. At the same electron energies as above, the tagged intervals are 14 and 20 MeV. A lead collimator with an aperture of 16 mm in diameter was used with the spectrometer with inclined pole faces. The tagging efficiency after collimation was measured with a Pb/SCIFI calorimeter [25] placed in the photon beam at low intensity. Efficiencies from 23% to 34% were obtained at the different photon energies, determined by the angular divergence of the bremsstrahlung beam. A collimator with an aperture of 12 mm was used for the Elbeck spectrometer and the efficiency of the measurement in the 50 MeV photon region with this spectrometer was 17%. The experiment in the giant dipole resonance region was performed with a mean tagging efficiency of 25%.

The product detectors were placed in an evacuated chamber with extending pipes sealed with 50 μm thick mylar foils. The entrance window was positioned 20 mm after the collimator. This gave a distance between the collimator and the center of the chamber of 780 mm. With additional lead shielding, the background contribution from the interaction between the beam and the air became negligible. The target frame within the chamber is attached to a rod which can be rotated 360 deg. The rod also can be raised and lowered providing an empty target area. Rectangular (80×60 mm) polystyrene foils $(C_8H_8)_n$ with areal densities of 26.30 mg/cm^2 and 26.56 mg/cm^2 were used in the quasideuteron (QD) region measurements. The thickness of the polystyrene target was chosen to be 16.50 mg/cm^2 for the GDR region due to the higher-energy loss in the target material for low-energetic protons. The chamber was lined up with Polaroid film positioned in frames at the entry and at the exit windows of the pipes. Interpolation from the photographs gave a beam spot of 11.5 mm diameter at the target position.

The chamber is designed to accommodate up to six Si-Ge telescopes at different angles, as shown in Fig. 1. The telescopes used consist of silicon ΔE detectors with a 900 mm^2 area and thickness of 500 μm, and hyperpure germanium E detectors with an area of 800 mm^2 and a thickness of 15 mm. With this system, it is possible to detect protons with a maximum kinetic energy of $\sim$60 MeV, which is sufficient for the present experiments. Each Si detector is 105 mm away from the center of the target, with an additional distance of 15 mm to the Ge detector, giving solid angles of order 55 msr per telescope. The Ge detectors are cooled with cold fingers connected to liquid nitrogen containers. A ^{228}Th source attached to the target frame is used for energy calibrations for all detectors. This is possible because the Si detectors are vertically mobile. The measurement in the GDR region differed from the other experiments with regard to the product detectors. Instead of telescopes, 4-mm-thick silicon E detectors, each with an area of 113 mm^2 were used. A distance of 106 mm from the center of the target to the back of the detectors resulted in a point source solid angle of 10 msr. The reduced solid angle was compensated for by the considerably higher cross sections in this energy domain.

DATA ANALYSIS

When using tagging spectrometers, each individual focal-plane detector defines a photo-nuclear experiment uncorre-

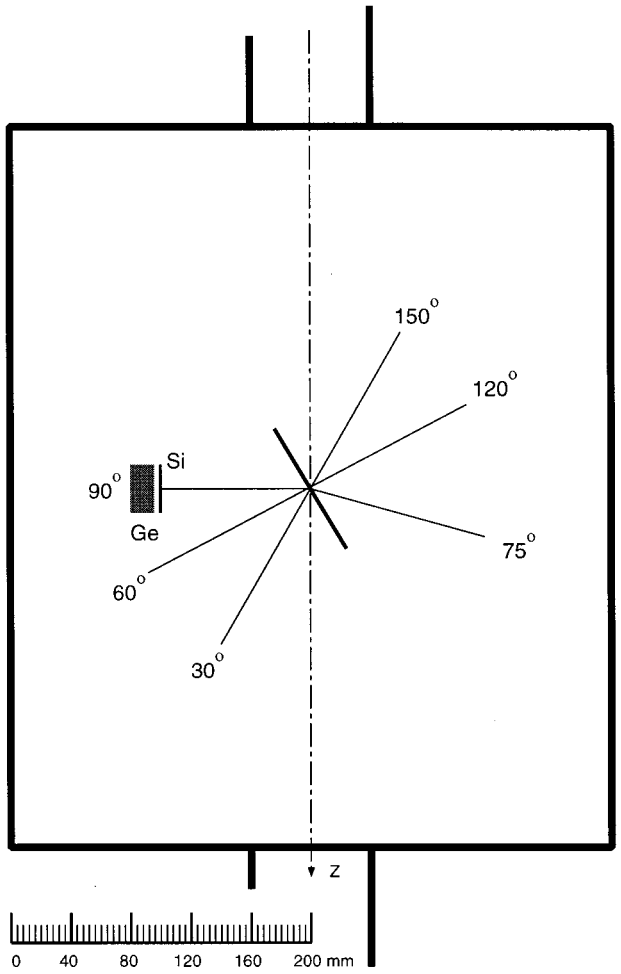

FIG. 1. One of the possible setups of the Gent-Lund-University-Experiments (GLUE) chamber is depicted from a top view. The target is set at 150° and the maximum number of Si-Ge telescopes is mounted. No support frames are shown for the detectors. On both sides, the detectors are connected through the support frames to base plates with cold fingers extending into two liquid-nitrogen containers below the chamber.

lated with the others. The analysis thus can be divided into two parts. The first consists of obtaining the kinetic energy of the reaction product at a defined detection angle, and the second of identifying the energy of the photon inducing the reaction.

In the calibrations of the reaction product detectors, the highest α-particle energy emitted from the source was 8.784 MeV. The maximum energy that could be detected in the silicon detectors was 12 MeV whereas for the germanium detectors, the highest energy that could be measured was 60 MeV. For the silicon detectors the calibrations were extremely stable when compared over a week. The extrapolation for the germanium detectors introduced an uncertainty of less than 1% in the detected energy. Different particles can be identified from the ΔE-E information by the T/a method [26] separating protons, deuterons, and tritons from electrons.

The missing energy E_m of the reaction is defined as

$$E_m \equiv E_\gamma - T_{B*} - T_p = (m_{B*} + m_p - m_C)c^2,$$

where E_γ is the photon energy, and T_p and T_{B*} are the kinetic energies of the ejectile, and residual nucleus, respectively. The masses of the residual nucleus, the ejectile and the target nucleus are denoted m_{B*}, m_p, and m_C respectively. Since the missing energy is invariant with respect to the photon energy, it allows summation of the spectra from several focal plane detectors. Considering the low cross sections, this is necessary in order to obtain statistically significant results.

Coincidences between product particles and residual electrons in the spectrometer are established to distinguish between protons with a correlated photon and those with uncorrelated residual electrons causing a background distribution. The proton starts the time measurement for all focal-plane detectors. With a suitable delay for the focal-plane detector signals, each individual coincidence measurement is stopped by the first residual electron detected in each detector. Correlated events will be centered around the chosen delay time in a time spectrum, superimposed on a background distribution, as shown in Fig. 2(c). The background distribution of accidental coincidences in the time interval containing correlated events is hatched in Fig. 2(c).

With appropriate time windows in Fig. 2(c), events belonging to the interval 51–63 ns may be selected. The missing energy is calculated for each proton resulting in a missing energy spectrum, Fig. 2(a), proportional to the number of events defined by the interval in the time spectrum. The hatched background distribution in the missing energy spectrum, corresponding to the hatched area in Fig. 2(c), is to be estimated.

Time intervals are chosen in the linear region on both sides of the peak area in the time spectrum in order to obtain a missing energy spectrum containing background contributions. An additional contribution of events due to noncorrelated electrons stopping the time measurement too early, when the photon actually had a correlated residual electron arriving later, will be included from the left of the peak area. This effect is dependent on the count rate of residual electrons and may be compensated for [27].

With one missing energy spectrum for the interval between 51 and 63 ns, and another one for the linear regions on both sides, a normalization of the proton yield may be carried out by the proportionality between the time spectrum intervals and the content of the missing energy spectra.

The background on either side of the peak in Fig. 2(c) is described by two linear functions obtained through least square fits. Intervals of 24 ns are used both to the left and to the right, excluding the nonlinear regions of 10 ns width in the immediate vicinity of the peak.

Once the extrapolated fitted functions have been summed for the area below the peak, and the background events have been summed for the time windows used, a normalization factor can be obtained as the ratio of the areas which are proportional to the missing energy spectra. Events generating overflows in the time spectrum were included in the missing energy spectrum in order to obtain a well-defined background. This was motivated by the identical energy distributions for uncorrelated protons within the time scale, and those generating overflows. The final normalization factor was calculated as the ratio between the number of events integrated below the peak interval, and the sum of events

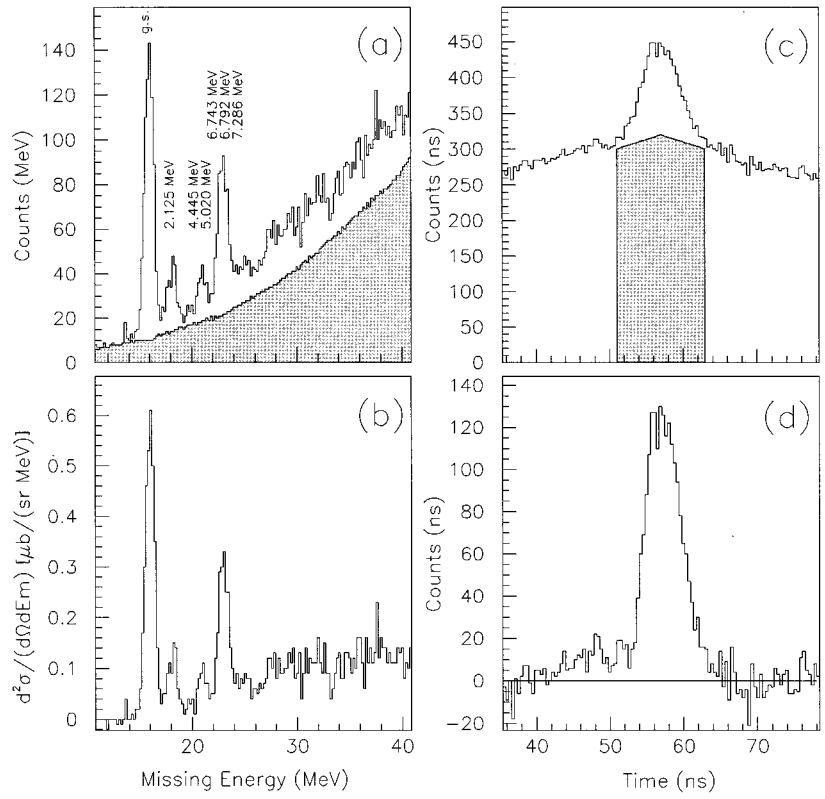

FIG. 2. The results in the figure were obtained with E_γ=75 MeV at a proton detection angle of 75°. The two discrete states in ^{11}B that can be resolved are shown. Two further states around $\sim$ 5 MeV and two unresolved states at $\sim$7 MeV excitation energy also can be distinguished. The hatched area of Fig. 2(a) shows the contribution from uncorrelated events, and the corresponding area is shown in the TOF spectrum, 2(c). Correlated and random events must be normalized based on the TOF spectrum, to give absolute differential cross sections as shown in 2(b). An estimate of the background contribution obtained from least-squares fits in 2(c) has been subtracted in 2(d). The FWHM of the individual states is approximately 1 MeV. Statistical uncertainties ($\sim$3%) are shown.

from both sides of the peak including all events with an overflow in the time spectrum. The normalized missing energy spectrum is shown in Fig. 2(b), together with the corresponding coincidence spectrum subtracted by the yield from the fitted functions, Fig. 2(d).

Figure 2(d) shows nonlinearities on both sides in the vicinity of the peak. An estimate of the systematic uncertainty was obtained by scaling the normalization factor from the calculated value with factors of 10 and 0.1, followed by another calculation of absolute differential cross sections. Since the uncertainty was of the order of 2%, the nonlinearities were not considered as important in the final results.

A Monte Carlo simulation was performed to obtain the solid angles of the telescopes. To obtain an estimate of systematic uncertainty, several random generators were used and a comparison with tables [28] showed that the total uncertainty was less than 3%. When the tagging efficiency of the spectrometer was measured before and after the experiment, the results differed at most by 5%, having negligible statistical uncertainty. The target angle is known within 3% and the polystyrene film used as target is manufactured with a tolerance of 2%. Assuming that the systematic uncertainties are independent, the root mean square is less than 8%.

In Fig. 3, absolute cross sections at 90° detection angle are compared with measurements [13,14,16,29–33] quoting overall systematic uncertainties around 20%. The abundance of data at photon energies between 52 and 63 MeV is shown as an inset in the upper-right panel of the figure. Apart from the measurements of Matthews *et al.* [13], all data were obtained with tagged photons. Different techniques were used to detect protons. Similar detectors (Si-strip ΔE and Ge E detectors) were used in Refs. [16,30,31], however, in Refs. [16,30] absolute cross sections were determined from the relative yields by normalizing the data to the results of Ref. [13]. The data presented in [13,14,29,31–33] are all absolute measurements. The comparison for the ground state at 90° proton detection angle shows that, when plotted logarithmically against the incident photon energy, the cross section decreases in the well-known linear fashion for photon energies below 100 MeV. No systematic difference can be seen for the results presented here, although the data were obtained in experiments performed over a three-year period with two different tagging spectrometers.

Simulation of the energy resolution that can be expected in the experiment has also been performed. Sources of uncertainty that were taken into account are the energy of the bremsstrahlung electron with respect to synchrotron losses, the width of the focal plane detectors measuring the rest electron energy, the target thickness, the angular uncertainty due to the solid angles of the telescopes (kinematic broadening), and the intrinsic resolution of the solid-state detectors. At a mean electron energy of 95 MeV, the major contributions come from the synchrotron radiation losses in the ring and the uncertainty in proton detection angle due to the solid angle of the telescopes. At 75 MeV the uncertainty in target losses becomes comparable to the contributions from the extension of the detectors and the losses in the stretcher ring. Without corrections for synchrotron radiation in the ring, the achievable experimental FWHM for the measured kinetic energy is $\sim$650 keV at 75 MeV and $\sim$1 MeV at 95 MeV, which agrees very well with the results of the simulation.

With the FWHM for the ground state in ^{11}B taken from a Gaussian fit, as shown in Fig. 4, a comparison can be made with Gaussians for the excitation energy regions of interest. The 2.125 MeV state has a FWHM that compares well with the ground state, but the distribution at $\sim$5 MeV has twice

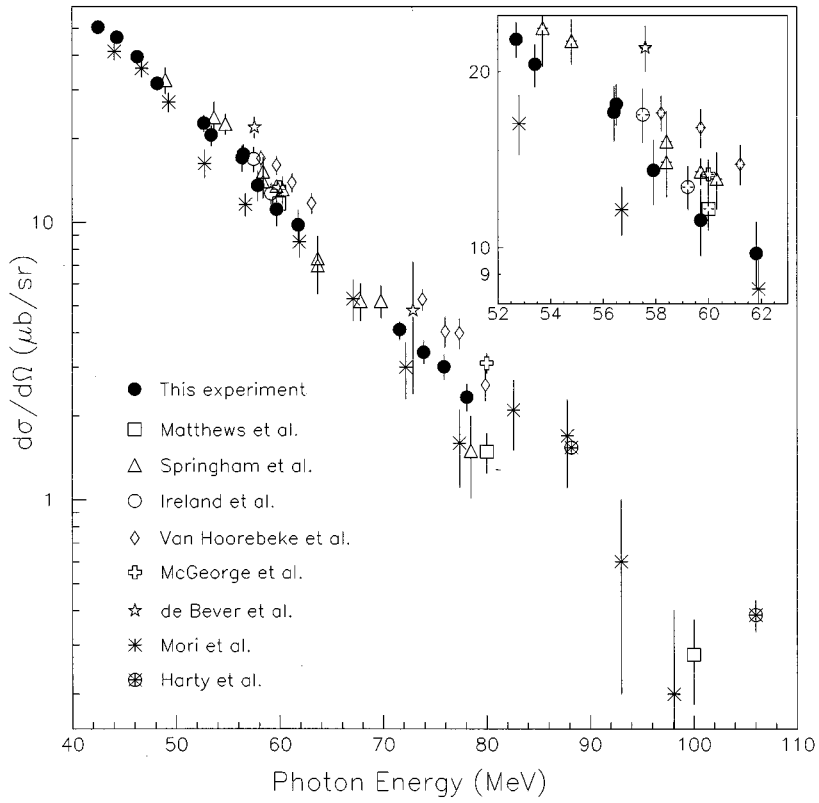

FIG. 3. All cross sections shown are for the sum of the ground state and the first excited state at a proton detection angle of 90°. The filled circles are data reported here. Open squares have been taken from Ref. [13]. The sets shown with open triangles [16] and open circles [30] were normalized to the results of Ref. [13]. The data represented by open diamonds are from Ref. [29] and were obtained with the same detectors as in the present experiment. The data shown as open crosses are from Ref. [14] and also represent absolute differential cross sections. The open stars represent data taken from Ref. [31]. The data shown with line crosses are from Ref. [32] and the line crosses within open circles from Ref. [33]. Statistical uncertainties are only shown.

the width. An attempt to resolve the two known states with fixed mean values and standard deviations taken from the ground state, results in approximately 30% of the strength for the unresolved 4.445 MeV state. Another interesting aspect is that the Gaussian at ~7 MeV excitation energy has the same FWHM as the ground state. This indicates that either the two states at ~6.8 MeV or the state at 7.3 MeV could be present. If all three states would be observed as one peak, its FWHM would be comparable with the width of the ~5 MeV states. The fits for the ~7 MeV region in the

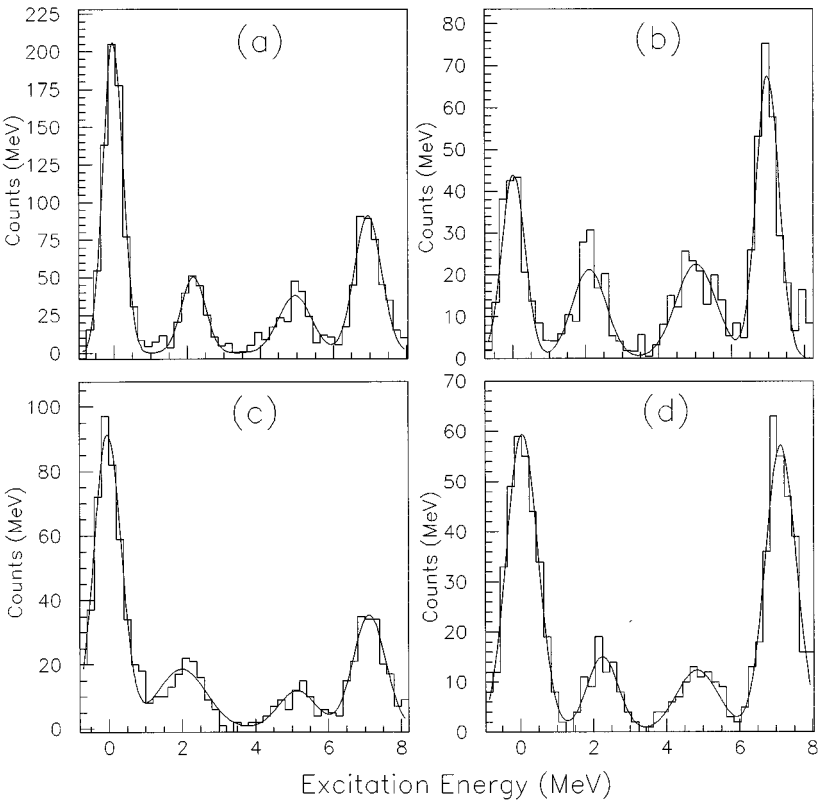

FIG. 4. Excitation energy spectra for ^{11}B: (a) E_γ=60 MeV, θ_p= 90°; (b) E_γ=60 MeV, θ_p= 120°; (c) E_γ=75 MeV, θ_p=60°; and (d) E_γ=75 MeV, θ_p= 90°. The FWHM's are similar for the ground state, the 2.125 MeV state, and the ~7 MeV states. At ~5 MeV the FWHM indicates excitation of two states.

missing energy spectra at the lower photon energies result in expectation values of the mean clearly indicating the presence of either the $(7/2^-)$ or $(1/2^+)$ state or both. At a photon energy of about 45 MeV, the 7-MeV peak is centered at 6.8 MeV with an uncertainty of about ± 50 keV. A slight nonlinearity in the energy calibration results in a shift upwards of the energies of excited states. At 75 MeV the peak is centered around 7 MeV with an uncertainty of ± 100 keV. The width of the 7-MeV states is equal to that of the ground state in the entire energy range investigated. The analysis has led to the conclusion that the ~ 7 MeV contribution is dominated by the $(7/2^-)$ and/or $(1/2^+)$ states.

RESULTS AND DISCUSSION

The measured cross sections with statistical uncertainties only are compiled in Tables I and II. Results for the $(3/2^-)$ ground state, the first excited state at 2.125 MeV $(1/2^-)$, the two unresolved states at 4.445 MeV $(5/2^-)$ and 5.020 MeV $(3/2^-)$, and the two unresolved states at 6.743 MeV $(7/2^-)$ and 6.792 MeV $(1/2^+)$, are presented in Table I as a function of mean photon energy and detection angle. Depending on the statistical significance, the averaging over focal-plane detectors giving the mean incident photon energy was different for forward and backward detection angles. For the measurements reported, the overall systematic uncertainty is lower than 8%. A mean was calculated for the overlapping cross sections from two data sets at 56.4 MeV mean photon energy. These data sets were obtained during two different experiments in 1990 and 1993, using two different tagging spectrometers. The difference in absolute cross sections was less than 4%, indicating that the systematic uncertainty is low. Table II presents the measured cross sections for the $(3/2^-)$ ground state with statistical uncertainties only for the giant dipole resonance (GDR) region. The systematic uncertainty for this data set was estimated to be 11%.

Figure 5 shows the cross sections determined in our experiments at 90° proton angle for the GDR and QD regions (left panel). The results for photon energies between 25 MeV and 30 MeV agree with previous measurements by the Gent group [34,35]. A steep decrease in the cross sections as a function of photon energy can be seen in the spectrum. The right upper panel shows some representative angular distributions for the GDR region. A peaking is apparent at about 80° detection angle and the distributions are symmetric. An almost flat plateau is observed in the photon energy interval between 37 MeV and 42 MeV, followed by a slower decrease in the cross sections in the QD region. The angular distribution is completely different for this region, as shown in the right lower panel of Fig. 5. A combination of data measured with photon energies at 37 MeV and 42 MeV scale quite well and the peak of the distribution is shifted towards 60° detection angle.

The (γ,p) reaction in the GDR region has been explained as a collective process dominated by 1-particle–1-hole (1p1h) states. However, the transition into the QD region has caused much debate concerning the possible reaction channels that contribute to the cross section. The direct coupling of the photon to the proton through the DKO mechanism in the QD region is contradicted by a recent comparison of $(e,e'p)$ and (γ,p) momentum distributions at equivalent missing momenta [36]. Parameters which describe the $(e,e'p)$ reaction as a DKO process are not applicable with respect to the (γ,p) reaction. Instead, it is suggested that MEC contribute to the (γ,p) cross section at the missing momenta probed. DKO calculations constrained by parameters deduced in a CDWIA analysis underestimate the (γ,p) cross sections by a factor of about 6 [36]. The discrepancy is largely removed by including meson exchange currents in a phenomenological way.

A direct evaluation of the exchange currents in the (γ,p) reaction was introduced by Gari and Hebach [10] in the 1970's. They used explicitly the complete Siegert operator in the evaluation of the transition matrix elements. The results implied important contributions from MEC to the (γ,p) cross section. Another method following the same principles of applying the Siegert theorem has been employed through self-consistent HF-RPA calculations with an effective Skyrme interaction by the Bologna group [11]. Within this model, the calculated cross sections for the target nuclei ^{16}O and ^{40}Ca also showed the importance of MEC contributions in explaining the experimental results.

In order to avoid the low-energy-limit approximation, the Siegert operator is not used in the HF-RPA calculations of the Gent group. The exchange current contributions are described in terms of the momentum dependence of the effective nucleon-nucleon interaction used in the calculations. Long-range correlations and multistep processes are treated within a continuum RPA framework. Collective properties of the target nucleus and rescattering effects thus were accounted for by the HF-RPA contribution whereas the contribution of MEC was added explicitly. With a different Skyrme force, having a stronger momentum dependence than the one used by Ref. [11], it was possible to reach the same agreement for (γ,p_0) and (γ,n_0) reactions on ^{16}O in the Gent model [12,37].

In this paper, the new $^{12}C(\gamma,p)$ data will be compared with calculations performed in a spherical continuum RPA framework. A spherical description of the target and residual nucleus is, of course, a simplification in the $^{12}C(\gamma,p)^{11}B$ reaction, but as it is the overlap of nuclear wave functions that is to be calculated, it has been assumed to be an acceptable approximation as both ^{12}C and ^{11}B are deformed.

The structure of the low-lying, odd-parity states in ^{11}B of the Gent model are assumed to be of the following form [19] (uncoupled version)

$$\begin{aligned}\langle {}^{11}B \otimes k_p | J_{[1]} + J_{[2]} | {}^{12}C(\text{g.s.}) \rangle \\ = \alpha \langle {}^{12}C(\text{g.s.}) | c^\dagger_{h_\pi} c_{p_\pi} (J_{[1]} + J_{[2]}) | {}^{12}C(\text{g.s.}) \rangle \\ + \beta \langle {}^{12}C(\text{g.s.}) | c^\dagger_{h_\pi} c^\dagger_{h_\nu} c_{p_\nu} c_{p_\pi} J_{[2]} | {}^{12}C(\text{g.s.}) \rangle\end{aligned}$$

where the one-body (and two-body) current operators are denoted by $J_{[1]}$ (and $J_{[2]}$) and h_π (and h_ν) refer to the quantum numbers of a proton (neutron) state. In the actual calculations, only the leading-term contributions to the wave functions were considered. Accordingly, the hole states are created exclusively in the $1p_{3/2}$ shell ($h_\pi = h_\nu = 1p_{3/2}$). In the photoabsorption process described by the first term, the proton is removed from the $1p_{3/2}$ shell and is excited into a continuum state. In the second term, both nucleons are re-

TABLE I. The measured cross sections (μb/sr) with statistical uncertainties only for the low-lying states in the residual ^{11}B nucleus. The systematic uncertainties are approximately 8%.

E_γ	θ_p	g.s.	2.125 MeV	5.020 MeV	~7 MeV
42.5	30.0	50.98±1.46	15.05±0.79	15.55±0.81	13.42±0.75
	60.0	66.56±1.68	12.46±0.73	12.00±0.71	11.45±0.70
	90.0	40.68±1.30	9.75±0.64	10.09±0.65	11.13±0.68
44.3	30.0	46.18±1.47	13.99±0.81	11.42±0.73	12.68±0.77
	60.0	60.32±1.69	16.68±0.89	7.49±0.59	14.23±0.82
	90.0	37.82±1.33	8.56±0.63	7.30±0.58	11.54±0.73
46.3	30.0	45.61±1.58	12.42±0.82	10.95±0.77	11.28±0.78
	60.0	55.81±1.75	11.30±0.79	8.45±0.68	19.59±1.04
	90.0	32.72±1.33	6.72±0.60	7.31±0.63	11.81±0.80
48.2	30.0	44.38±1.50	11.84±0.77	11.94±0.78	11.49±0.76
	60.0	50.09±1.59	12.64±0.80	8.42±0.65	11.06±0.75
	90.0	25.14±1.12	6.46±0.57	5.61±0.53	11.27±0.75
52.7	30.0	35.22±1.45	11.08±0.81	11.20±0.82	9.65±0.76
	60.0	39.73±1.54	9.96±0.77	5.88±0.59	10.62±0.80
	90.0	16.82±1.00	5.92±0.59	5.69±0.58	8.95±0.73
53.4	30.0	32.36±1.63	9.53±0.88	8.29±0.83	9.94±0.90
	60.0	33.58±1.67	9.76±0.90	4.47±0.61	11.33±0.97
	90.0	16.25±1.15	4.33±0.59	1.88±0.39	8.49±0.83
56.4	30.0	27.80±1.68	8.62±0.93	7.71±0.88	6.80±0.76
	60.0	31.98±1.64	8.20±0.84	6.26±0.73	8.25±0.83
	90.0	13.56±1.23	3.48±0.63	3.61±0.63	6.13±0.83
	120.0	2.87±0.48	1.06±0.30	1.72±0.38	3.69±0.55
56.5	30.0	28.88±1.35	8.01±0.71	9.27±0.76	6.49±0.64
	60.0	31.06±1.40	8.51±0.74	4.95±0.56	8.00±0.71
	90.0	13.54±0.92	4.07±0.51	3.64±0.48	6.14±0.62
57.9	30.0	22.59±1.59	6.83±0.87	12.42±1.18	7.66±0.81
	60.0	30.74±1.55	6.94±0.75	6.22±0.75	9.32±0.86
	90.0	10.58±1.12	2.98±0.60	3.11±0.61	6.47±0.88
	120.0	1.95±0.39	1.87±0.38	1.32±0.32	3.11±0.49
59.1	120.0	2.13±0.26	1.36±0.21	1.48±0.22	3.43±0.34
	150.0	0.45±0.09	0.47±0.09	1.69±0.17	1.56±0.16
59.7	30.0	19.70±1.44	6.36±0.82	6.77±0.85	5.29±0.66
	60.0	27.03±1.42	6.84±0.72	4.45±0.58	8.54±0.80
	90.0	9.33±1.02	1.80±0.44	1.99±0.48	5.79±0.81
	120.0	1.77±0.36	0.66±0.22	1.25±0.30	3.68±0.52
61.8	30.0	16.82±1.21	4.48±0.62	5.69±0.70	5.37±0.60
	60.0	23.64±1.20	6.52±0.63	3.81±0.49	6.91±0.65
	90.0	7.75±0.85	2.03±0.43	1.61±0.39	3.77±0.59
	120.0	1.26±0.28	0.90±0.23	1.98±0.35	2.34±0.38
71.6	30.0	9.10±0.38	2.90±0.22	1.57±0.16	2.91±0.22
	60.0	10.19±0.63	3.16±0.35	1.30±0.23	3.67±0.38
	75.0	7.47±0.34	1.57±0.16	1.22±0.14	4.52±0.27
	90.0	3.34±0.23	0.76±0.11	0.96±0.12	2.80±0.21
	120.0	0.43±0.09	0.22±0.06	0.26±0.07	1.55±0.16
73.9	30.0	8.32±0.39	2.40±0.21	2.34±0.21	3.03±0.23
	60.0	8.62±0.62	1.80±0.28	0.85±0.20	3.77±0.41
	75.0	7.33±0.36	1.49±0.16	1.33±0.15	3.94±0.27
	90.0	2.76±0.23	0.64±0.11	0.61±0.11	2.61±0.22
	120.0	0.15±0.05	0.25±0.07	0.54±0.10	1.18±0.15
74.7	150.0	0.07±0.04	0.27±0.07	0.80±0.12	1.74±0.18
75.9	30.0	6.81±0.35	1.61±0.17	1.65±0.17	2.69±0.22
	60.0	7.78±0.59	1.47±0.26	1.56±0.26	4.32±0.44
	75.0	5.31±0.31	1.17±0.14	1.22±0.15	4.06±0.27
	90.0	2.36±0.21	0.65±0.11	0.33±0.08	2.19±0.20
	120.0	0.34±0.08	0.04±0.03	0.42±0.09	0.93±0.13
78.1	30.0	6.09±0.32	1.48±0.16	0.93±0.12	1.63±0.12
	60.0	7.77±0.57	1.50±0.25	0.67±0.17	2.55±0.33
	75.0	4.40±0.27	1.13±0.14	0.53±0.09	2.80±0.22
	90.0	1.74±0.17	0.60±0.10	0.41±0.08	2.56±0.21
	120.0	0.29±0.07	0.14±0.05	0.18±0.06	0.73±0.11

TABLE II. The measured cross sections (μb/sr) with statistical uncertainties only for the ground state in the residual ^{11}B nucleus. The systematic uncertainties are approximately 11%.

	θ_p				
E_γ	40.0	60.0	80.0	100.0	120.0
25.1	312±27	495±25	553±26	514±26	381±22
27.5	224±25	291±22	323±23	250±21	172±17
29.9	124±16	221±16	228±16	199±15	118±12
37.2	52±7	68±5	57±5	30±3	16±3

moved from the $1p_{3/2}$ orbit. The neutron then is excited into the $1p_{1/2}$ orbit and the proton is excited into the continuum. The potential for the shell model calculations is defined as spherically symmetric and the wave functions are generated in a shell model for the A-nucleon system [38]. Ground-state correlations are effectively included in the first term in the RPA calculation.

The first term in the expression above refers to the one-hole components of the $(A\text{-}1)$ nucleus. This component can be reached through both the one-body (IA) and the two-body (MEC) currents. The two-body part of the current also can feed 2h1p components (second term in the above expression) in the wave function of the final nucleus. As the contributions from the different wave function components add coherently when computing the squared transition matrix elements, the predicted cross section depends strongly on the values and the relative signs of the wave function amplitudes α and β. It is clear that in order to obtain a complete description of the final state, several 2h1p components must be considered. In the approach of Ref. [19], however, only the leading 2h1p component in the final state has been retained. For the higher unresolved negative-parity states, the excitations generally will be of 2h1p type, or result in more complicated nh(n-1)p configurations which are not included in the model at present. These higher-order nh(n-1)p configurations ($n \geqslant 3$) can be reached only through n-body ($n \geqslant 3$) absorption mechanisms or through complicated FSI effects.

A comparison between the Gent model results and the data presented here for the $(3/2^-)$ ground state and the second $(3/2^-)$ state shows for the first time that the cross sections have different signatures for backward angles in the (γ,p) reaction. Compared with the $(e,e'p)$ reaction, where the results are similar for the two $(3/2^-)$ states, an interesting property of the results plotted in Figs. 6 and 7 is the qualitative behavior of the angular distributions for the two states. While the ground state angular cross section [Fig. 6(a)] decreases strongly with increasing proton detection angle, the $\sim$5 MeV states [Fig. 6(b)] exhibit a different structure with a possible increase at the highest measured angle partly due to the contribution from the $(5/2^-)$ state. The observed difference between the angular behavior for the two $(3/2^-)$ states is reasonably reproduced in the model calculations.

In Fig. 7(a), calculations for the ground state which is known to be of mainly 1h character are compared with measurements at photon energies of 75 MeV. The general shape of the data is not fully reproduced at backward angles where the experimental cross sections indicate a steep decline, whereas the theoretical cross sections overestimate the cross sections. For the first excited state in ^{11}B shown in Fig. 7(b),

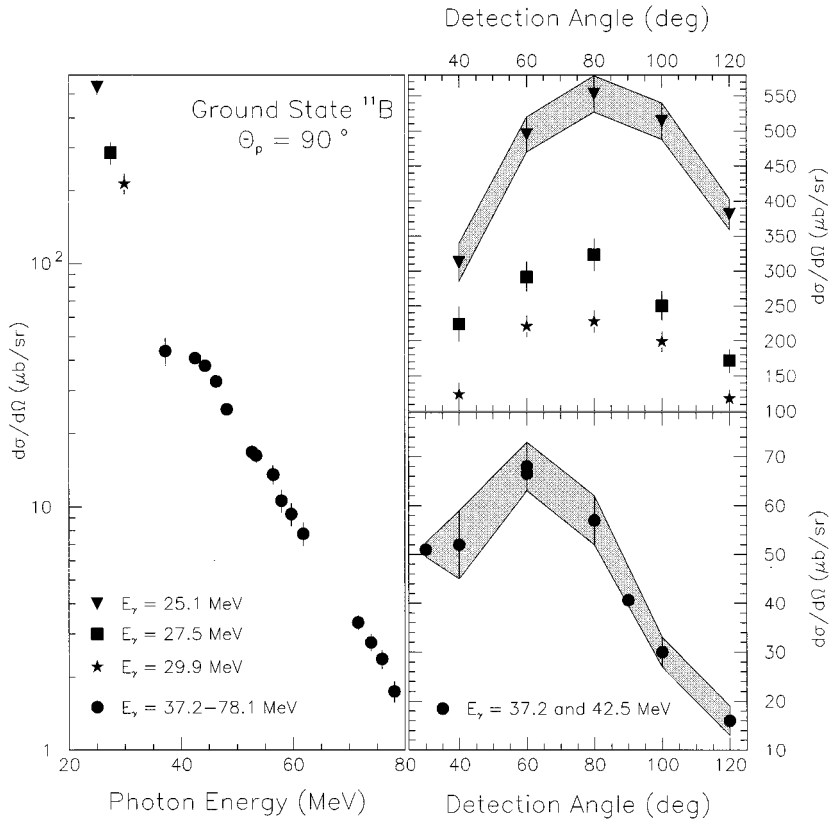

FIG. 5. Cross sections for transitions to the $(3/2^-)$ ground state in ^{11}B are shown with only statistical uncertainties. The left panel shows the data collected in this study from the GDR and the QD region. In the upper-right panel the angular distribution for the GDR region is shown and the corresponding distribution for the QD region is shown in the lower-right panel.

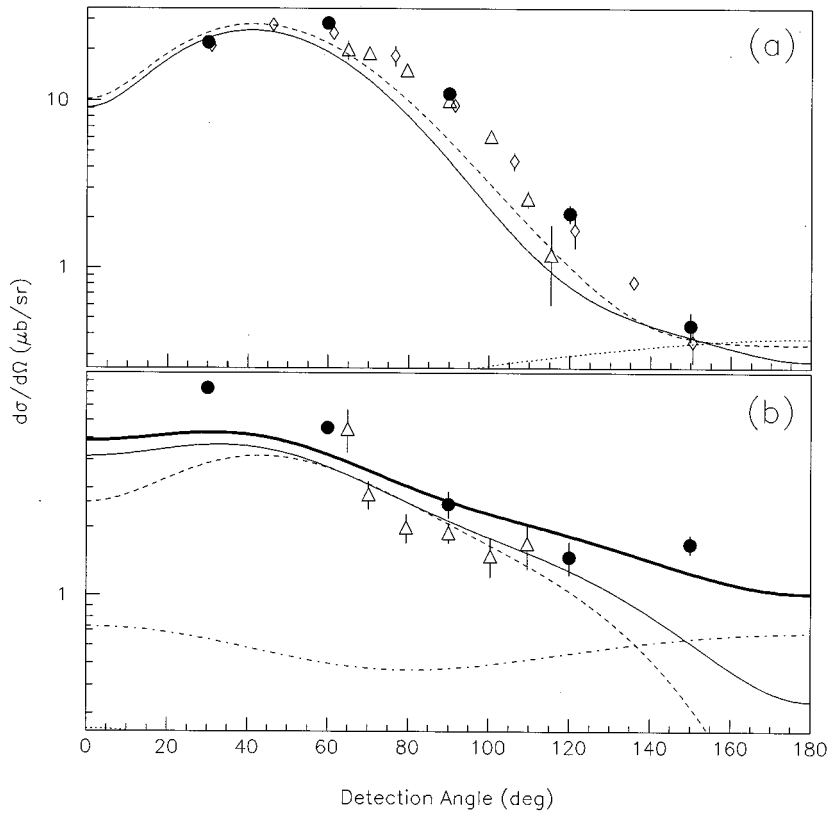

FIG. 6. Calculations for an incident photon energy of 60 MeV are compared with measured data. Panel (a) shows the ground state with contributions from 1h matrix elements as a dashed line, the 2h1p exchange-current part as a dotted line, and their coherent sum as a solid line. In panel (b) the measured data are for the two unresolved states $(3/2^-)$ and $(5/2^-)$ at ~ 5 MeV. The equivalent line types are used for the second $(3/2^-)$ state. In addition, the contribution from the $(5/2^-)$ state is shown with a dot-dashed line. The incoherent sum of the contributions for both states is shown with a thick solid line. The angular distributions shown as filled circles are from the present work, open diamonds are from Ref. [13], and the open triangles have been taken from [16]. The statistical uncertainties are comprised within the data points for those not showing error bars. Refer to the text for further details.

the coherent sum of mainly 1h and weak 2h1p contributions gives a good description of the data with regard both to the amplitude and the distribution. Calculations for the 5.020 MeV state in Fig. 7(c) show the growing importance of one-pion exchange currents at higher excitation energies in the residual nucleus. The squared wave function amplitude $|\alpha|^2$, describing the hole state contributions, is large in the computation for the ground state [$\alpha = 0.69$ taken from QE $(e,e'p)$ results in Refs. [39,40]] whereas it is comparatively small for the second $(3/2^-)$ state ($\alpha = 0.22$). This part of the

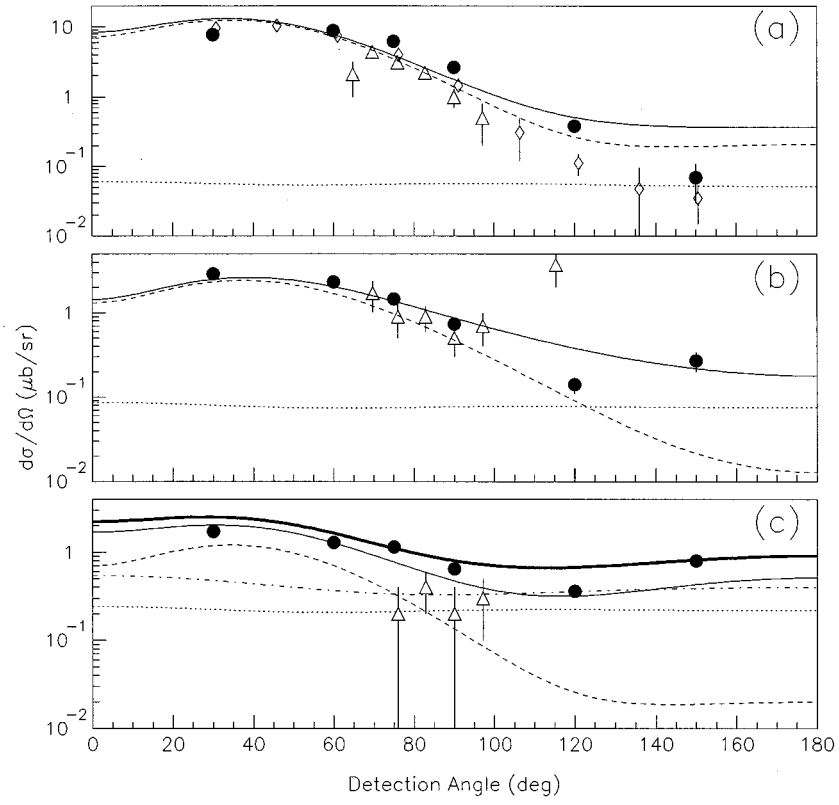

FIG. 7. Calculations for an incident photon energy of 75 MeV showing the contributions from the different states with line types according to Fig. 6 are compared with measured data. Panel (a) shows the $(3/2^-)$ ground state, panel (b) the first excited state $(1/2^-)$ at 2.125 MeV, and panel (c) the second $(3/2^-)$ and the $(5/2^-)$ states at ~ 5 MeV. The experimental cross sections are from the same references as in Fig. 6. Refer to the text for further details.

squared matrix element (dashed lines in Fig. 7) generates most of the cross section for the ground state and provides the shape of the angular distribution in the forward angles. As opposed to the ground state, only a weak contribution from the same shape is seen for the second $(3/2^-)$ state. Furthermore, $|\beta|^2$ is small for the ground state and large for the second $(3/2^-)$ state and the squared matrix element (dotted lines in Fig. 7), in general, contributes via a constant magnitude over the proton angular range. As the contributions are coherently summed (solid lines in Fig. 7) the resulting distributions are largely due to interference effects. Thus, the rise in the theoretical cross section for backward angles shown in Fig. 7(c) is mainly due to interference effects between the 1h and 2h1p components of the squared matrix elements. This contribution is computed with regard to the sign of the wave function amplitude $2\alpha\beta$.

In a previous section, it was indicated that approximately 30% of the measured cross section for the ~5 MeV excitation energy region was due to the 4.445 MeV state. The $(5/2^-)$ state in ^{11}B at 4.445 MeV has not been identified in the previous (γ,p) experiments. As large admixtures of $1f$ components in the wave function for the ground state of ^{12}C can be ruled out, it cannot be explained with a one-step reaction process. Previous $(e,e'p)$ experiments have not shown any observable strength for the $(5/2^-)$ state either, but in a recent measurement under nonparallel conditions, the first observation was reported [41]. Already at a missing momentum of 182.5 MeV/c in the $(e,e'p)$ reaction in nonparallel kinematics, the increased similarity to the (γ,p) reaction is claimed to be seen. The two-step contribution exceeds the DKO component by two orders of magnitude in the calculations for the $(5/2^-)$ state. Also, pickup reactions such as $(p,2p)$, $(d,^3He)$, and $(t,^4He)$ [42–44] show excitation of the $(5/2^-)$ state. Two-step processes within a DWIA or DWBA model is the suggested explanation of the excitation in the hadron reactions.

An alternative explanation for the excitation of the $(5/2^-)$ state in reactions induced by real photons is suggested in the Gent model. As the 1h component is extremely small, it is assumed to be of mainly 2h1p character. A feeding of the $(5/2^-)$ state may be obtained by photoabsorption on a two-body MEC operator. Calculated cross sections for the $(5/2^-)$ state are shown in Figs. 6 and 7. The predicted magnitude of the angular cross section (dot-dashed line) is relatively independent of the detection angle for the proton, in agreement with the 2h1p contributions to the $(3/2^-)$ states. The thick solid lines in Figs. 6(b) and 7(c) show the incoherent sum of the calculated cross sections for the second $(3/2^-)$ and the $(5/2^-)$ states. In line with the conclusions from the analysis of the spectra, the $(5/2^-)$ contribution constitutes a considerable fraction of the total strength measured for the two states.

In the Gent model, the even-parity states in ^{11}B are described by 2h1p contributions only

$$\beta\langle^{12}C(\text{g.s.})|c^\dagger_{h_\pi}c^\dagger_{h_\nu}c_{p_\nu}c_{p_\pi}J_{[2]}|^{12}C(\text{g.s.})\rangle.$$

In this matrix element, the neutron is propagated into the $1d_{5/2}$ or the $2s_{1/2}$ orbit. As for the odd-parity states, only the leading terms in the final state wave function are included in the actual computation.

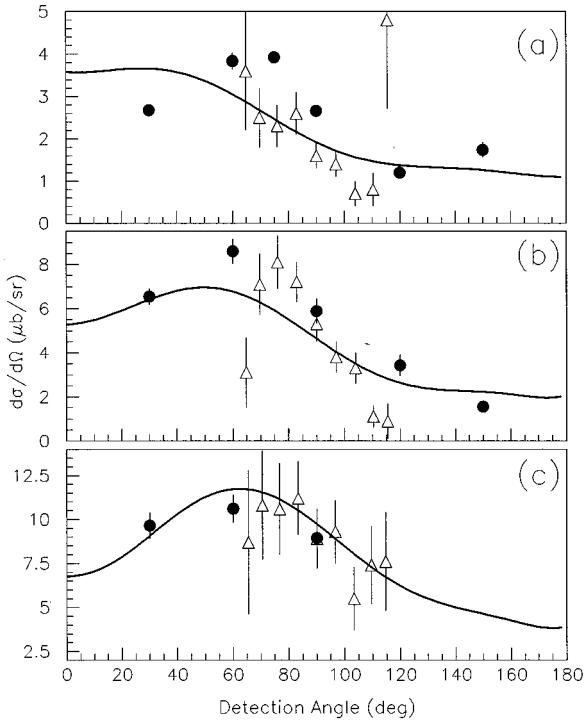

FIG. 8. The calculated angular distributions for the excited states at ~7 MeV, based on two-body absorption only [19], are compared to experimental results. The symbols used for the data points are the same as in Fig. 6. Panel (a) is a comparison at E_γ~75 MeV, panel (b) at E_γ~60 MeV, and panel (c) at E_γ~50 MeV. Refer to the text for further details.

A previous experiment [29] for the (γ,p) experiment at incident photon energies of 61 and 77 MeV indicated that three unresolved states at ~7 MeV excitation energy in ^{11}B contributed to the cross section [18]. Since the states at ~7 MeV excitation energy were unresolved, it was difficult to predict cross sections as the relative importance of the states was difficult to estimate. Also, it is generally believed that the reaction mechanism is different from that of the lower-lying excited states. Theoretical curves from calculations [19] including 2h1p contributions are shown only in Fig. 8. Figure 8(a) shows a comparison at E_γ~75 MeV, 8(b) at E_γ~60 MeV, and 8(c) at E_γ~50 MeV. An increase in the importance of the higher-order electric multipole operators as the transferred impulse of the photon becomes larger can be seen for forward angles in the calculated distributions. However, the data indicate that the peak of the distributions is fairly constant, around 60° proton detection angle as the incident photon energy increases, in contradiction to the theoretical results. The magnitude of the cross sections, as well as the general shape of the data at a lower photon energy, are, however, quite well reproduced. In Ref. [19] the calculated cross section is presented as the incoherent sum of the cross sections to each of the three states. The agreement seen in Figs. 8(b) and 8(c) seems to be fortunate as the Gent model predicts a dominance of the $(5/2^+)$ state for this region of photon energy. The contributions to the calculated cross sections from the two states that we observe experimentally, i.e., the $(7/2^-)$ and $(1/2^+)$ states, result in a flat angular distribution at, e.g., 60 MeV. A reinterpretation of

the calculations presented in Ref. [19] thus is required.

From the present data, we conclude that the 7-MeV peak is dominated by contributions from the $(7/2^-, 1/2^+)$ doublet. The fact that the $(5/2^-)$ state also contributes to the excitation energy spectra points to the importance of two-step processes in this reaction in a similar way as in the $(e,e'p)$ reaction [40]. The effects of deformation also should be considered as both ^{12}C and ^{11}B are deformed [45–47].

CONCLUSIONS

The systematic measurements of the $^{12}C(\gamma,p)^{11}B$ reaction presented here have revealed that the $(5/2^-)$ state is excited in contrast to previous results. A reinterpretation of the results obtained in Ref. [19] has led to the inclusion of the $(5/2^-)$ state in the model calculations in the present paper. For the states at ~ 7 MeV excitation energy, it is shown that the cross sections obtained are due to the unresolved $(7/2^-)$ and $(1/2^+)$ states. It is, at present, impossible to explain the strong excitation of the ~ 7 MeV excitation region without including the $(5/2^+)$ state in the model. Other discrepancies remain, especially at forward angles for the emitted proton. A comparison with the $^{12}C(\gamma,n)$ reaction [48] shows that there is a close similarity to the (γ,p) reaction in the cross sections obtained, and this supports the argument of one-pion exchange currents as an important effect in photon-induced reactions below the pion threshold. The agreement of the model calculations by the Gent group with the $^{12}C(\gamma,n)$ measurements is rather poor, and it is clear that further theoretical work is necessary in order to describe the measured data.

An experimental contribution would be to resolve the three states around 7 MeV in excitation energy in the residual ^{11}B nucleus with new $(\gamma,p\gamma')$ coincident experiments [49] as it is difficult to obtain higher-energy resolution with the present (γ,p) and (γ,n) experiments. Measurements at higher missing momenta for the $(e,e'p)$ reaction would be of great interest, as they would allow a more direct comparison of the reaction mechanisms involved. As it is well known that the DKO reaction dominates at the available $p_m < 200$ MeV/c, comparisons with the available $(e,e'p)$ data are hampered by the fact that real photon-induced reactions are performed at $p_m > 300$ MeV/c.

ACKNOWLEDGMENTS

The authors would like to thank the staff of the MAX laboratory for their help and assistance during the experiments. Financial support from the Swedish Natural Science Research Council is gratefully acknowledged, as well as support by the Knut and Alice Wallenberg Foundation, the Crafoord Foundation, the Swedish Institute, and the contribution from the Royal Swedish Academy of Sciences. The Gent collaborators were supported by the Interuniversity Institute of Nuclear Science and the National Fund for Scientific Research in Belgium.

[1] L.S. Cardman, University of Illinois Report P/83/12/168, 1983.
[2] J.L. Matthews, *Lecture Notes in Physics* (Springer, New York, 1979), Vol. 108, p. 369.
[3] S. Boffi, F. Cannata, F. Capuzzi, C. Giusti, and F.D. Pacati, Nucl. Phys. **A379**, 509 (1982).
[4] S. Boffi, C. Giusti, and F.D. Pacati, Nucl. Phys. **A359**, 91 (1981).
[5] S. Boffi, R. Cenni, C. Giusti, and F.D. Pacati, Nucl. Phys. **A420**, 38 (1984).
[6] S. Boffi, F. Capuzzi, C. Giusti, and F.D. Pacati, Nucl. Phys. **A436**, 438 (1985).
[7] B. Schoch, in *Proceedings of the Fourth Course of the International School of Intermediate Energy Nuclear Physics*, 1983, San Miniato, Italy, edited by R. Bergere, S. Costa, and C. Schaerf (World Scientific, Singapore, 1984) p. 189.
[8] H. Schier and B. Schoch, Nucl. Phys. **A229**, 93 (1974).
[9] H. Göringer and B. Schoch, Phys. Lett. **97B**, 41 (1980).
[10] M. Gari and H. Hebach, Phys. Rep. **72**, 1 (1981).
[11] M. Cavinato, M. Marangoni, and A.M. Saruis, Nucl. Phys. **A422**, 237 (1984).
[12] J. Ryckebusch, M. Waroquier, K. Heyde, J. Moreau, and D. Ryckbosch, Nucl. Phys. **A476**, 237 (1988).
[13] J.L. Matthews, D.J.S. Findlay, S.N. Gardiner, and R.O. Owens, Nucl. Phys. **A267**, 51 (1976).
[14] J.C. McGeorge *et. al.*, Phys. Lett. B **179**, 212 (1986).
[15] A.C. Shotter, S.V. Springham, D. Branford, J. Yorkston, J.C. McGeorge, B. Schoch, and P. Jennewein, Phys. Rev. C **37**, 1354 (1988).
[16] S.V. Springham *et al.*, Nucl. Phys. **A517**, 93 (1990).
[17] L. Van Hoorebeke *et al.*, Phys. Rev. C **42**, R1179 (1990).
[18] D. Nilsson *et al.*, Phys. Scr. **49**, 397 (1994).
[19] J. Ryckebusch, K. Heyde, L. Machenil, D. Ryckbosch, M. Vanderhaeghen, and M. Waroquier, Phys. Rev. C **46**, R829 (1992).
[20] M. Eriksson, Nucl. Instrum. Methods **196**, 331 (1982).
[21] L.J. Lindgren and M. Eriksson, Nucl. Instrum. Methods **214**, 179 (1983).
[22] L.J. Lindgren and M. Eriksson, Nucl. Instrum. Methods Phys. Res. A **294**, 10 (1990).
[23] J-O. Adler *et al.*, Nucl. Instrum. Methods Phys. Res. A **294**, 15 (1990).
[24] I. Anthony, J.D. Kellie, S.J. Hall, and G.J. Miller, Nucl. Instrum. Methods Phys. Res. A **301**, 230 (1991).
[25] D.W. Hertzog, S.A. Hughes, P.E. Reimer, R.L. Tayloe, K.F. Johnson, S. Majewski, C. Zorn, and M. Zorn, University of Illinois Report P/90/7/88, 1990.
[26] F.S. Goulding, D.A. Landis, J. Cerny, and R.H. Pehl, Nucl. Instrum. Methods **31**, 1 (1964).
[27] R.O. Owens, Nucl. Instrum. Methods Phys. Res. A **288**, 574 (1990).
[28] A.V.H. Masket, R.L. Macklin, and H.W. Schmitt, Oak Ridge National Laboratory Report ORNL-2170, 1956.
[29] L. Van Hoorebeke, Ph.D. thesis, University of Gent, 1991.
[30] D.G. Ireland *et al.*, Nucl. Phys. **A554**, 173 (1993).
[31] L.J. de Bever, Ph.D. thesis, NIKHEF-K, 1993.
[32] K. Mori *et al.*, Phys. Rev. C **51**, 2611 (1995).
[33] P.D. Harty *et al.*, Phys. Rev. C **51**, 1982 (1995).

[34] E. Kerkhove, P. Berkvens, R. Van de Vyver, D. Ryckbosch, P. Van Otten, H. Ferdinande, E. Van Camp, and A. De Graeve, Phys. Rev. C **33**, 1796 (1986).
[35] R. Van de Vyver (private communication).
[36] D.G. Ireland and G. van der Steenhoven, Phys. Rev. C **49**, 2182 (1994).
[37] G.J. Miller *et al.*, Nucl. Phys. **A586**, 125 (1995).
[38] E. Warburton and J. Millener (private communication).
[39] G. van der Steenhoven, H.P. Blok, E. Jans, M. de Jong, L. Lapikas, E.N.M. Quint, and P.K.A. de Witt Huberts, Nucl. Phys. **A480**, 547 (1988).
[40] G. van der Steenhoven, H.P. Blok, E. Jans, L. Lapikas, E.N.M. Quint, and P.K.A. de Witt Huberts, Nucl. Phys. **A484**, 445 (1988).
[41] I. Bobeldijk, H.P. Blok, and G. van der Steenhoven, Phys. Lett. B **281**, 25 (1992).
[42] D.W. Devins, D.L. Friesel, W.P. Jones, A.C. Attard, I.D. Svalbe, V.C. Officer, R.S. Henderson, B.M. Spicer, and G.G. Shute, Aust. J. Phys. **32**, 323 (1979).
[43] G. Mairle and G.J. Wagner, Nucl. Phys. **A253**, 253 (1975).
[44] O. Karban, A.K. Basak, J.B.A. England, G.C. Morrison, J.M. Nelson, S. Roman, and G.G. Shute, Nucl. Phys. **A269**, 312 (1976).
[45] S.G. Nilsson, Mat. Fys. Medd. Dan. Vidensk. Selsk. **29**, 16 (1955).
[46] H.-B. Håkansson, T. Berggren, and R. Bengtsson, Nucl. Phys. **A306**, 406 (1978).
[47] I. Ragnarsson, S. Åberg, H.-B. Håkansson, and R.K. Sheline, Nucl. Phys. **A361**, 1 (1981).
[48] J.R.M. Annand, G.I. Crawford, P.D. Harty, J.C. McGeorge, G.J. Miller, B-E. Andersson, J-O. Adler, S.A. Bulychjev, L. Isaksson, H. Ruijter, and B. Schrøder, Phys. Rev. Lett. **71**, 2703 (1993).
[49] M. Thompson *et al.*, MAX-LAB Activity Report, 1995.